FACULTY
OF MATHEMATICS
AND PHYSICS
Charles University

SUMMARY OF DOCTORAL THESIS

Helena Žlebčíková

Anisotropic tomography of the European upper mantle

Department of Geophysics

Supervisor of the doctoral thesis: RNDr. Jaroslava Plomerová, DrSc.
Study programme: Physics
Specialization: Geophysics

Prague 2018

MATEMATICKO-FYZIKÁLNÍ
FAKULTA
Univerzita Karlova

AUTOREFERÁT DIZERTAČNÍ PRÁCE

Helena Žlebčíková

Anizotropní tomografie svrchního pláště pod Evropou

Katedra geofyziky

Vedoucí dizertační práce: RNDr. Jaroslava Plomerová, DrSc.
Studijní program: Fyzika
Studijní obor: Geofyzika

Praha 2018

Dizertace byla vypracována na základě výsledků získaných v letech 2011-2018 během doktorandského studia na Katedře geofyziky MFF UK, v Geofyzikálním ústavu AV ČR a během studijních pobytů na ETH Zürich.

Dizertant:
Mgr. Helena Žlebčíková
Geofyzikální ústav AV ČR
Boční II 1401, 141 31 Praha 4

Školitel:
RNDr. Jaroslava Plomerová, DrSc.
Geofyzikální ústav AV ČR
Boční II 1401, 141 31 Praha 4

Oponenti:
Prof. Ulrich Achauer
Institut de physique du globe de Strasbourg
École et observatoire des sciences de la Terre
Université de Strasbourg
5 rue René Descartes, 67084 Strasbourg Cedex, France

Dr. Nicola Piana Agostinetti
Department für Geodynamik und Sedimentologie
Fakultät für Geowissenschaften, Geographie und Astronomie
Universität Wien
Althanstraße 14, 1090 Wien, Österreich

Předsedkyně oborové rady:
doc. RNDr. Hana Čížková, Ph.D.
Katedra Geofyziky MFF UK
V Holešovičkách 2, 180 00 Praha 8

Obhajoba dizertace se koná dne 1. 3. 2019 v 10:00 hodin před komisí pro obhajoby dizertačních prací v oboru Geofyzika v přednáškovém sále Geofyzikálního ústavu AV ČR, v.v.i., Boční II 1401, Praha 4.

S dizertací je možno se seznámit na oddělení postgraduálního studia MFF UK, Ke Karlovu 3, Praha 2, a na webové stránce www.ig.cas.cz/obhajene-prace.

Contents

1. Introduction

Anisotropy of seismic-wave velocities of the Earth's upper mantle is a key source contributing to deciphering tectonic history of the lithosphere-asthenosphere system (e.g., Babuška & Cara 1991; Šílený & Plomerová 1996; Silver 1996; Savage 1999; Park & Levin 2002; Fouch & Rondenay 2006; Mainprice 2007; Maupin & Park 2007; Long & Silver 2009; Long & Becker 2010). Large-scale anisotropy, detectable by seismic waves passing through the Earth, occurs as a consequence of lattice-preferred orientation (LPO) of the intrinsically anisotropic minerals, particularly olivine and pyroxene, constituting the upper-mantle rocks. The LPO reflects the stress field acting when the rocks were ductile, i.e., the stress field in the time of a mantle-lithosphere origin (e.g., Babuška & Plomerová 1989) or a current stress field in the case of asthenosphere (e.g., Silver & Chan 1991; Savage 1999). The effective strength of the large-scale upper-mantle anisotropy is lower than the intrinsic anisotropy of the individual minerals (e.g., Christensen 1984).

While sub-horizontally propagating surface waves can provide us with integral and long-wavelength variations of the upper-mantle anisotropy, body waves, i.e., shear waves and particularly P waves, are sensitive to smaller-size structures due to their shorter wavelengths and broad angles of steeper propagations. Thus, the P waves can supply us with relatively detailed information on the upper-mantle fabrics (e.g., Babuška & Plomerová 1992; 2006). Nevertheless, most of the standard teleseismic body-wave tomography studies neglect the P-wave anisotropy although such a simplification is incongruous with the current understanding of the upper-mantle dynamics. Moreover, ignoring the seismic anisotropy can produce artefacts in the resulting purely isotropic-velocity models (e.g., Sobolev *et al.* 1999; Menke 2015; Bezada *et al*. 2016).

Various tomographic approaches that do not fully neglect anisotropy appeared in the past and their number has been increasing recently (e.g., Hirahara & Ishikawa 1984; Eberhart-Phillips & Henderson 2004; Ishise & Oda 2005; 2008; Wang & Zhao 2008; 2012; Tian & Zhao 2013; Ishise *et al.* 2015; Koulakov *et al.* 2015; Liu & Zhao 2016; 2017). However, they are mostly limited to the crust, using local-earthquake datasets and searching for azimuthal anisotropy only. On the other hand, e.g., Hua *et al.* (2017) or Gou *et al.* (2018) evaluate also radial anisotropy from merged local-earthquake and teleseismic datasets, i.e., travel times or travel-time residuals of P waves, but the separation of the radial and azimuthal anisotropy yet represents a significant simplification of the true anisotropic structure of the Earth.

Confining orientation of the symmetry axis to horizontal (in azimuthal anisotropy) or vertical (in radial anisotropy) directions does not conform to path-integrated anisotropic characteristics inferred from teleseismic body waves observed in tectonically different continental provinces (e.g., Babuška *et al.* 1984; 1993; Babuška & Plomerová 2006; Plomerová & Babuška 2010; Plomerová *et al.* 2011; 2012). The authors demonstrate dependence of SKS-wave splitting parameters and P-wave travel-time residuals on direction of wave propagation, taking into account both azimuth and incidence angles. Such characteristics with a general 2π periodicity imply a need to treat anisotropy in 3D. Self-consistent anisotropic models of continental mantle lithosphere usually document that derived symmetry axes of the anisotropic domains are oriented generally in 3D, i.e., inclined from horizontal (e.g., Plomerová *et al.* 2012).

To contribute to studies of the large-scale anisotropy of the upper mantle, we have developed a novel code called AniTomo for regional coupled anisotropic-isotropic tomography as a modification of code Telinv for regional isotropic-velocity tomography (e.g., Weiland *et al.* 1995; Arlitt *et al.* 1999; Sandoval *et al.* 2004; Karousová *et al.* 2013; Plomerová *et al.* 2016). The AniTomo code inverts travel-time residuals of teleseismic P waves simultaneously for 3D distribution of the isotropic-velocity perturbations and anisotropy assuming weak anisotropy with hexagonal symmetry oriented generally in 3D. The code represents a step further from modelling homogeneously anisotropic blocks of the mantle lithosphere (e.g., Plomerová *et al.* 2002; Vecsey *et al.* 2007; Plomerová *et al.* 2011) towards modelling anisotropy arbitrarily varying in 3D. The current version of AniTomo is applicable only to P waves and not to S waves, for which anisotropic propagation is much more complex.

We have tested the new code thoroughly, involving both simple methodological tests to find out basic characteristics of the method and tests mimicking real tomographic inversions as to the target structures and the station-event distribution. For the first application of the AniTomo code to a real dataset, we have selected data from international passive seismic experiment POLENET/LAPNET that was deployed in northern Fennoscandia between 2007 and 2009 (e.g., Kozlovskaya 2007). The north-eastern part of the Fennoscandian Shield is an assemblage of micro-plate nuclei, island arcs, terranes and mobile belts of prevailingly Archean age (e.g., Snyder 2002; Korja *et al.* 2006; Lahtinen *et al.* 2015). At present, northern Fennoscandia is a tectonically stable region with a relatively thick lithosphere (Plomerová & Babuška 2010) and without significant thermal heterogeneities (e.g., Slagstad *et al.* 2009, for a review).

2. Theory and description of code AniTomo

We aim at modelling anisotropic upper-mantle structures with the use of teleseismic P-wave tomography. The crucial part of the theory is a derivation of an explicit formula for P-wave velocities in weakly anisotropic medium with hexagonal symmetry and the symmetry axis oriented generally in 3D. Then, linearization of the relation between data, i.e., travel-time residuals, and model parameters describing the anisotropic medium is straightforward.

2.1 P-wave velocity in weakly anisotropic medium with hexagonal-symmetry axis generally oriented in 3D

Backus (1965) applied first-order expansion of Christoffel equation for propagation of plane waves in homogeneous anisotropic elastic medium and he found an approximate but explicit formula for body-wave velocity v in weakly anisotropic medium with a general symmetry

$$v = c + \frac{B^{(1)}}{2c}, \qquad (1)$$

where c is wave velocity in isotropic medium and $B^{(1)}$ is the 1st order perturbation of the non-degenerated eigenvalue of Christoffel tensor. Particularly for P waves, $B^{(1)}$ can be expressed as

$$B^{(1)} = \gamma_{ijkl} n_i n_j n_k n_l \,, \tag{2}$$

where γ_{ijkl} are small variations of isotropic density-normalized elastic coefficients adjusting for the weak anisotropy. Vector $\boldsymbol{n}$ represents a propagation direction of the P wave.

Implementing hexagonal symmetry into equation (2), the anisotropic velocity gains a form of

$$v = \bar{v}\left(1 + \frac{k}{2}\cos 2\alpha\right), \tag{3}$$

where $\bar{v}$ is isotropic component of anisotropic velocity, k is strength of anisotropy and α is an angle between the symmetry axis and wave-propagation direction.

As AniTomo employs only P-wave and no S-wave travel times, we cannot recover the five elastic coefficients of the anisotropy with assumed hexagonal symmetry individually, but only their combinations. We translate these combinations into isotropic component of velocity $\bar{v}$ and strength of anisotropy k, which can be expressed as

$$\bar{v}^2 = \frac{1}{8\rho}\left[3(A+C) + 2(F+2L)\right], \tag{4}$$

$$k = \frac{4(C-A)}{3(A+C) + 2(F+2L)}\,, \tag{5}$$

where ρ is density and A, C, F and L are elastic coefficients. Positive values of strength of anisotropy correspond to hexagonal symmetry with axis a in direction of high velocity (call high-velocity a axis), perpendicular to low-velocity plane (b,c), and vice versa - negative values correspond to hexagonal symmetry with axis b in direction of low velocity (call low-velocity b axis), perpendicular to high-velocity plane (a,c).

In order to transform angle α into a ray-parameter coordinate system, we define orientation of the symmetry axis by unit vector $\boldsymbol{s}$ and propagation direction of the wave by unit vector $\boldsymbol{n}$ as

$$\boldsymbol{s} = (\sin\theta \sin\lambda\,, \sin\theta \cos\lambda\,, \cos\theta), \tag{6}$$

where λ and θ are azimuth and inclination (measured upward from vertical) of the symmetry axis and

$$\boldsymbol{n} = (-\sin i \sin\varphi\,, -\sin i \cos\varphi\,, -\cos i), \tag{7}$$

where φ and i are back-azimuth and incidence angle of the wave propagation. After substituting $\cos 2\alpha = 2\cos^2\alpha - 1$ and $\cos\alpha = \boldsymbol{n}\cdot\boldsymbol{s}$ in equation (3), the P-wave velocity in weakly anisotropic medium with hexagonal symmetry and a general orientation in 3D can be expressed as

$$v = \bar{v}\left\{1 + k\left[\left(\sin i \sin\theta\cos(\varphi-\lambda) + \cos i\cos\theta\right)^2 - \frac{1}{2}\right]\right\}. \tag{8}$$

This equation relates anisotropic velocity v of a P wave propagating in a direction given by angles φ and i with isotropic component $\bar{v}$ of the anisotropic velocity and the directionally variable velocity perturbation, i.e., the term with strength of anisotropy k.

2.2 System of linearized equations

Similarly to the isotropic tomography, AniTomo needs a linearized relation between travel-time residual Δt and model parameters, i.e., perturbations of the parameters describing the anisotropic medium $\Delta\bar{v}$, Δk, $\Delta\lambda$ and $\Delta\theta$,

$$\Delta t = \sum_j \left(\frac{\partial t}{\partial \bar{v}}\right)_j \Delta\bar{v}_j + \sum_j \left(\frac{\partial t}{\partial k}\right)_j \Delta k_j + \sum_j \left(\frac{\partial t}{\partial \lambda}\right)_j \Delta\lambda_j + \sum_j \left(\frac{\partial t}{\partial \theta}\right)_j \Delta\theta_j, \tag{9}$$

where index *j* denotes contribution to the travel-time residual from the jth ray segment. The travel time t of a P wave in the anisotropic medium is

$$t = \frac{s}{v(\bar{v}, k, \lambda, \theta)}, \tag{10}$$

where $v(\bar{v}, k, \lambda, \theta)$ stands for the anisotropic velocity (eq. 8). Partial derivatives of the travel time with respect to the anisotropic parameters in equation (9) are then

$$\frac{\partial t}{\partial \bar{v}} = -\frac{s}{v_0 \cdot \bar{v}_0}, \tag{11}$$

$$\frac{\partial t}{\partial k} = -\frac{s}{v_0}\cdot\left[\left(\sin i \sin\theta_0 \cos(\varphi-\lambda_0) + \cos i\cos\theta_0\right)^2 - \frac{1}{2}\right], \tag{12}$$

$$\frac{\partial t}{\partial \lambda} = -\frac{s}{v_0}\cdot 2k_0\left(\sin i \sin\theta_0 \cos(\varphi-\lambda_0) + \cos i\cos\theta_0\right)\cdot \sin i \sin\theta_0 \sin(\varphi-\lambda_0), \tag{13}$$

$$\frac{\partial t}{\partial \theta} = -\frac{s}{v_0}\cdot 2k_0\left(\sin i \sin\theta_0 \cos(\varphi-\lambda_0) + \cos i\cos\theta_0\right)\cdot \left(\sin i \cos\theta_0 \cos(\varphi-\lambda_0) - \cos i \sin\theta_0\right)$$
. (14)

As the partial derivatives depend on the anisotropic parameters, the problem is still non-linear. Thus, we fix the anisotropic parameters in equations (11-14) to the reference

values (marked with index 0) and solve the problem iteratively. The reference values come from the initial model during the first iteration and from the model resulting after the (n-1)th iteration during the nth iteration.

Equation (9) established for all the station-event P-wave travel-time residuals forms a system of linearized equations that we iteratively solve with the damped least-square method (Menke 1984)

$$\boldsymbol{m} = (\mathbf{A}^{\mathbf{T}}\mathbf{W}_{\mathbf{D}}\mathbf{A} + \varepsilon^2\mathbf{W}_{\mathbf{M}})^{-1}\mathbf{A}^{\mathbf{T}}\mathbf{W}_{\mathbf{D}}\boldsymbol{d}, \tag{15}$$

where $\boldsymbol{m}$ is a vector of model parameters $\Delta\bar{v}$, Δk, $\Delta\lambda$ and $\Delta\theta$ at all grid nodes. Data vector $\boldsymbol{d}$ contains travel-time residuals Δt and matrix $\mathbf{A}$ stores the partial derivatives from equation (9). Observation errors are considered in weighting matrix $\mathbf{W}_{\mathbf{D}}$. Damping factor ε^2 and horizontal smoothing $\mathbf{W}_{\mathbf{M}}$ stabilize the ill-posed problem. All these matrices have a block structure. During the calculations, the inverse in equation (15) is approximated by truncated singular value decomposition and 3D bending technique Simplex (Steck & Prothero 1991) is applied for the ray-tracing.

2.3 Brief description of code AniTomo

The developed coupled anisotropic-isotropic tomography code (AniTomo) has been created as a modification of widely-used code Telinv for high-resolution regional isotropic tomography of the upper mantle from residuals of travel times of teleseismic body waves. Telinv is a Fortran code originally developed by J. Taylor, E. Kissling, U. Achauer, C. M. Weiland and L. Steck. It has been used and modified by many authors (e.g., Weiland et al. 1995; Arlitt et al. 1999; Lippitsch et al. 2003; Sandoval et al. 2004; Shomali et al. 2006; Eken et al. 2007; Karousová et al. 2012; 2013; Plomerová et al. 2016; Silvennoinen et al. 2016; Chyba et al. 2017). Actual updated version of the Telinv code can be downloaded from http://www.ig.cas.cz/en/research-teaching/software-download/.

AniTomo is a new and unique code for regional travel-time tomography of the upper mantle. Travel-time residuals of teleseismic P waves are inverted both for anisotropic and isotropic velocity models described by parameters of weak anisotropy with hexagonal symmetry. These model parameters are perturbations of isotropic component of anisotropic velocity, strength of anisotropy and general orientation of the symmetry axis in 3D defined by its inclination and azimuth. Directionally dependent velocities of wave propagation are evaluated according to equation (8) whenever it is required, e.g., during ray tracing or calculation of the partial derivatives of travel times. Equation (8) is valid only for P waves in weakly anisotropic media with hexagonal symmetry and axes oriented generally in 3D. Thus AniTomo can not be used for S waves, for which anisotropic propagation is more complex.

To adapt the original isotropic code for its anisotropic version, we enlarge number of unknown parameters, because we iteratively search for up to four model parameters at each node of a 3D orthogonal grid. Due to the increased complexity, good ray coverage of the model in terms of number and directional distribution of the rays is crucial for reliable results of the inversion. In order to express 3D distribution of the rays within the parameterization cells, we implemented in AniTomo calculations of ray density tensor (Kissling 1988; Sandoval et al. 2004). The code is written in such a way that we can fix

any parameter when it is not well determined. Thus, we can limit anisotropic inversion only to a well-resolved part of the volume studied and run isotropic inversion in the remaining volume simultaneously. Purely isotropic inversion is also possible with AniTomo.

3. Synthetic testing of novel anisotropic teleseismic body-wave tomography code AniTomo

3.1 Setup of the synthetic experiment

We have evaluated many different synthetic tests to investigate an influence of various parameters controlling the inversion on the results. In this chapter, we show an example of synthetic tests that focus on setting an initial anisotropic model.

The synthetic model consists of three blocks, two of which are anisotropic (north-western and southern) and one (north-eastern) is purely isotropic. All the three blocks extend from 45 km down to 135 km and they are characterized by different isotropic components of the anisotropic velocity (Fig. 1 and Tab. 1). The anisotropic blocks possess 5 % anisotropy with different orientations of the symmetry axes. The isotropic velocities are non-perturbed above and below the three blocks. Such a synthetic model of sharply bounded anisotropic blocks is motivated by a concept of continental mantle lithosphere formed as an assemblage of lithospheric domains, preserving their mean velocities and fossil fabrics (e.g., Plomerová & Babuška 2010).

There is a spacing of 30 km between the grid nodes both horizontally and vertically, resulting in 8 x 8 x 8 nodes, in which the unknown model parameters are searched. Synthetic set of 9504 rays corresponds to P waves propagating from 66 equally-distributed teleseismic events to 144 stations located at the surface above the volume studied. The input dataset for the synthetic tests of AniTomo consists of travel-time residuals calculated as differences between the travel times of P waves passing through the synthetic structure and the travel times calculated for the IASP’91 reference model.

	Vel. pert. from IASP'91 (%)	Strength of anisotropy (%)	Azimuth of symmetry axis (°)	Inclination of symmetry axis (°)
North-western b.	3	5	120	50
North-eastern b.	- 3	0	NA	NA
Southern b.	0	5	0	30

Table 1. Anisotropic parameters of the three anisotropic blocks of the synthetic model mimicking domains of continental mantle lithosphere (see Fig. 1). Shortcut vel. pert. stands for velocity perturbation and b. for block.

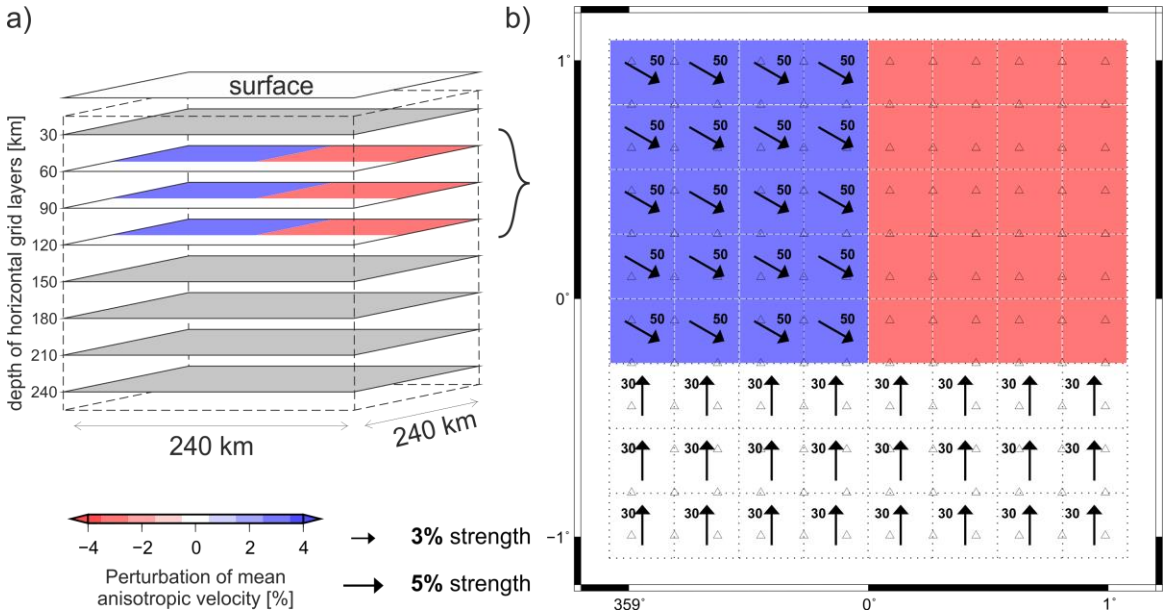

Figure 1. Scheme of synthetic model mimicking a realistic anisotropic structure of the mantle lithosphere (a). Three blocks with different anisotropy and isotropic component of velocity (b) are put between depths of 45 km and 135 km. Both the north-western high-velocity and the north-eastern low-velocity blocks exhibit 3 % amplitude of the isotropic-velocity perturbations. Strength of anisotropy in the north-western and in the southern blocks is 5 %. The arrows indicate strength of anisotropy and azimuth of orientation of the symmetry axis at the parameterization nodes. In general, we plot the arrows only for anisotropy stronger than 1 %. Axis inclination measured upward from vertical is marked with a number next to the arrow. A case of a low-velocity symmetry axis would be marked with 'b', otherwise the axis is high-velocity. The horizontal distribution of parameterization cells is marked with dotted lines.

We repeat the inversion several times, always with a different initial orientation of the symmetry axis, i.e., initial azimuth of 0º, 90º, 180º and 270º, and inclination of 10º - sub-vertical axis, 45º - dipping axis and 80º - sub-horizontal axis. By such a procedure, we minimize a danger that the resulting model combined from all the individual solutions is affected by an initial setup of the symmetry-axis orientation. The initial isotropic component of velocity corresponds to the IASP'91 reference model and the initial strength of anisotropy is 1 %.

3.2 Results of the synthetic experiment

Fig. 2 shows output model parameters at depth of 90 km from inversions with different initial angles of azimuth and inclination: with initial symmetry axis inclined at 45º and successively at azimuths of 0º (a), 90º (b), 180º (c) and 270º (d), with a sub-vertical axis orientation of 10º inclination and azimuth of 0º (e) and a sub-horizontal orientation of 80º inclination and azimuth of 90º (f). Anisotropy in the north-western block characterized by axis inclining 50º from vertical in azimuth of 120º (see Fig. 1 and Tab. 1) is well recovered for the initial models with inclined initial axis in azimuth of 90º (Fig. 2b) or 180º (Fig. 2c) and also for the initial model with the sub-horizontal axis gently dipping in azimuth of 90º (Fig. 2f). In the case of the other two initial orientations of inclined axes (at azimuth of 0º

and 270º) the recovered model is more complex and does not capture well the anisotropy of the synthetic model. At some nodes, even solutions with low-velocity *b* axis occur despite the fact that the target anisotropy is of a high-velocity *a* axis (Figs 2a and d). Such a solution appears when the initial orientation of the symmetry axis is far from the true high-velocity *a* axis of the synthetic model and it is thus closer to the low-velocity (*b*,*c*) plane of the prescribed hexagonal anisotropy. In the southern block, anisotropy inclined at 30º in azimuth of 0º is recovered well by inversions with the initial inclined or sub-vertical symmetry axes both in azimuth of 0º (Figs 2a and e).

The sensitivity of resulting models on initial anisotropic parameters calls for being careful when setting the initial parameters for anisotropic tomography. To minimize any potential bias, while modelling the a-priori unknown anisotropic structure of the Earth's upper mantle, we have looked for a way how to evaluate and present a whole family of anisotropic model parameters retrieved in each node for the set of initial setups. Fig. 3 combines all the output models in such a way that the isotropic components of velocity resulting from all the inversions are averaged at individual nodes, while the output strength of anisotropy, the azimuth and inclination of the symmetry axis are displayed individually for each inversion and every grid node. To present the retrieved anisotropy at each node, we plot its strength in stereographic projection on the lower hemisphere, where the two angles represent orientation of the symmetry axis.

The three blocks of the synthetic model can be easily distinguished at the depth of 90 km according to all the model parameters. In the north-western block of the model, the resulting orientations of the high-velocity *a* axis (blue symbols) tend to concentrate in roughly south-eastern inclined directions (within dashed green curve; Fig. 3), which is in agreement with the target anisotropy in the north-western block. On the other hand, there are also low-velocity *b* axes (red symbols) that incline in approximately opposite, i.e., in the north-western directions. These 'secondary' solutions with the low-velocity *b* axis have a very similar distribution of directions of relatively high and low velocities for teleseismic P waves as the target anisotropy with high-velocity *a* axis. Preference of the models with *b* axis is a consequence of a large angular deviation between the corresponding initial axes and the target symmetry axis. Distribution of the solutions with a low-velocity *b* axis complements at each node the solutions with a high-velocity *a* axis, confirming thus self-consistency and stability of the anisotropic part of the model.

In the south (within dotted green curve), the resulting high-velocity *a* axes concentrate correctly in directions steeply inclined toward the north. On the other hand, the north-eastern region does not exhibit distinct signs of anisotropy. The strength of anisotropy is low there (1 - 2 %) and orientations of the output axes are rather diffuse than localized. This indicates that the coupled anisotropic-isotropic inversion does not create any coherent anisotropy in the isotropic north-eastern part of the model. In general, structure of the blocks is well recovered and the resulting model captures perfectly sharpness of the block boundaries.

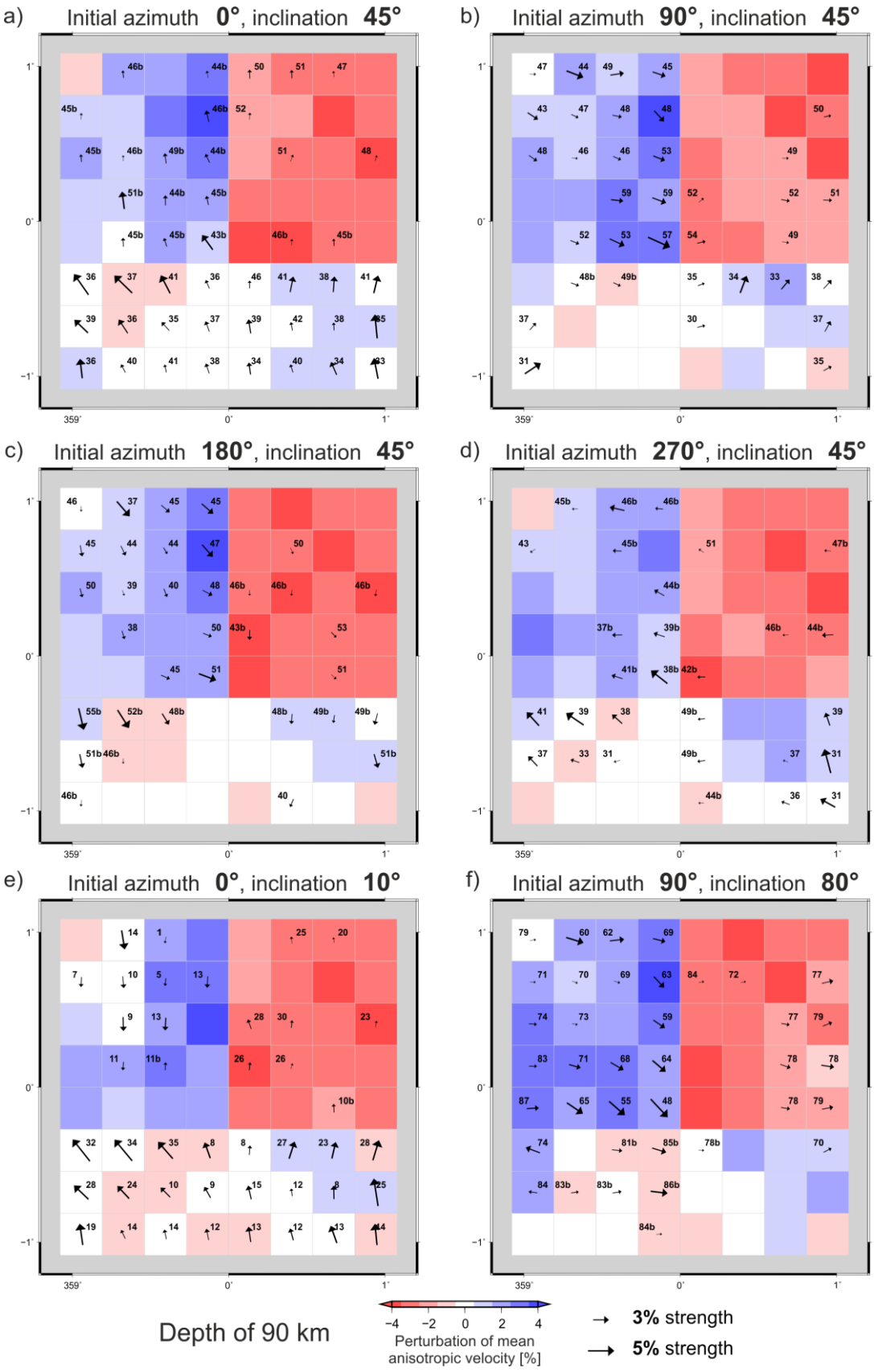

Figure 2. Resulting model parameters at 90 km depth after four iterations of synthetic inversions with different initial orientations of the symmetry axis. See Fig. 1 for the synthetic model and for description of visualization of the anisotropic parameters.

Contrast between the resulting parameters at the depth of 90 km and those at 150 km, representing the topmost isotropic layer below the anisotropic blocks, is evident (Fig. 3). Some leakage of both the isotropic and anisotropic components of velocity below the anisotropic blocks appears due to smearing along the ray paths, which is a typical drawback of teleseismic tomography, but it does not exceed amplitude of 2 % of isotropic perturbations and anisotropy strength. Moreover, concentration of symmetry axes toward a particular direction is very limited and it appears only in a few grid cells or at the model edges indicating an artefact. Results of the synthetic test allows us to conclude that running the anisotropic inversion systematically for different initial orientations of the symmetry axis leads to a robust model of anisotropic velocities.

We performed also many synthetic tests to investigate well-known trade-off between anisotropy and isotropic-velocity variations. To summarize them, the coupled anisotropic-isotropic inversion does not tend to create anisotropic artefacts when the real structure is purely isotropic. In the case of anisotropic structure, the situation is more complex. A part of the anisotropic contribution to velocity might be misinterpreted either as an isotropic component or as localized, usually weaker, anisotropy smeared into the isotropic part. Nevertheless, regions of distinct anisotropy and isotropic-velocity heterogeneities are identified correctly. Such findings represent a great benefit of the coupled anisotropic-isotropic inversion compared to a purely isotropic inversion, which misinterprets the anisotropic signal completely.

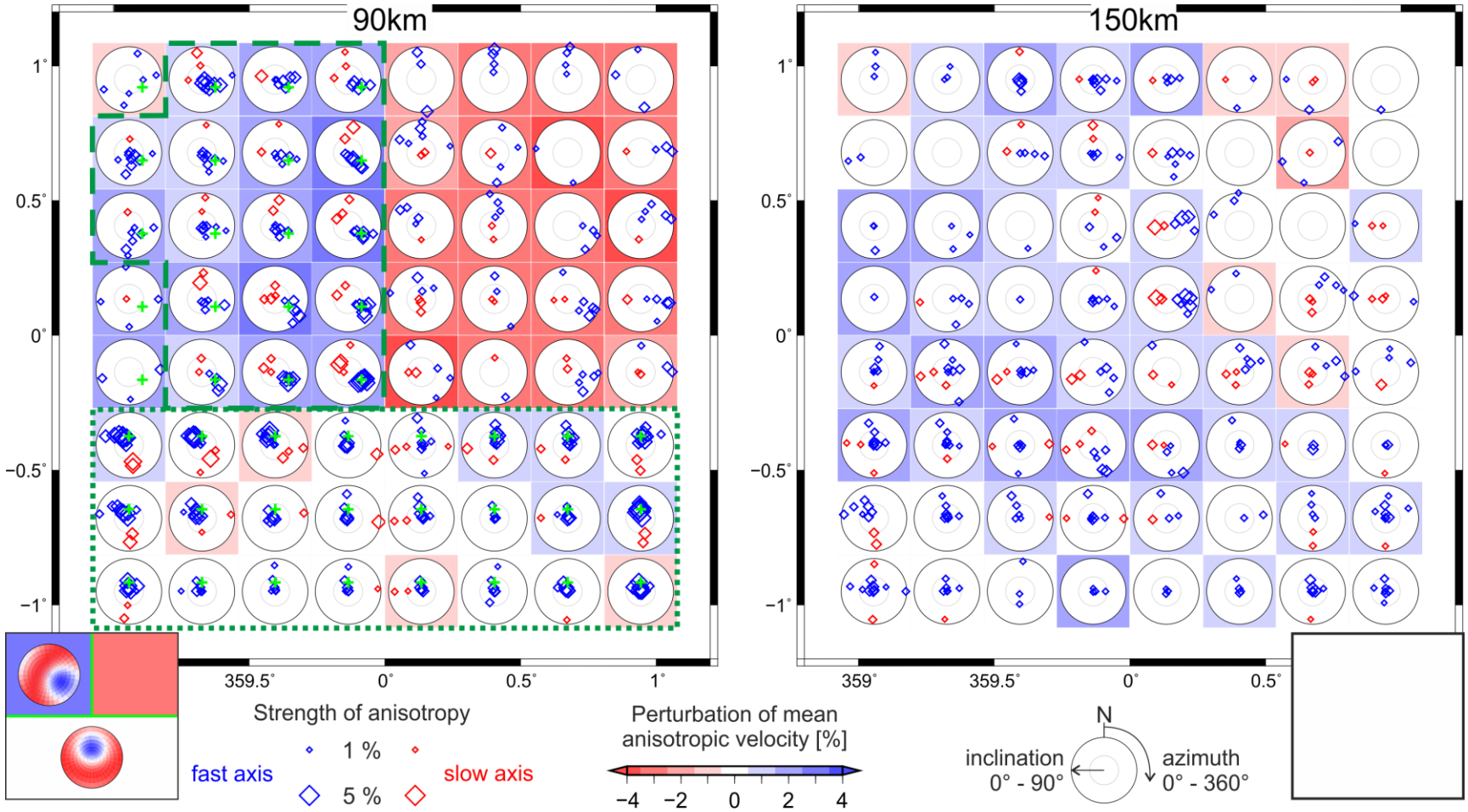

Figure 3. Resulting model parameters after four iterations of synthetic inversions with different initial orientations of the symmetry axis imaged together in the combined output model at 90 km and 150 km depths. The isotropic components of velocity from the individual inversions are averaged at each node and displayed as background squares. Output orientations from the individual inversions are imaged as single points at each node represented by blue or red symbols for high-velocity *a* or low-velocity *b* axis of hexagonal symmetry, respectively, in lower-hemisphere stereographic projection (white circles). Size of the symbols is scaled by strength of anisotropy and only parameters with strength larger than 1 % are plotted, because resolution of symmetry-axis orientation decreases with decreasing strength of anisotropy. The synthetic, i.e., correct orientations of symmetry axis are marked with green crosses at nodes where non-zero strength is assigned in the synthetic model. The insets also schematically image the input synthetic structure. Dashed, or dotted, green curves delimit regions that exhibit a relatively homogeneous anisotropy associated with the north-western, or southern, block of the synthetic model, respectively.

4. Application of novel anisotropic teleseismic body-wave tomography code AniTomo to data of passive seismic experiment LAPNET in northern Fennoscandia

4.1 Data pre-processing and setup of the inversion

Seismic array LAPNET (e.g., Kozlovskaya 2007; http://www.oulu.fi/sgo-oty/lapnet/; http://www.fdsn.org/networks/detail/XK_2007/) was installed on the territory of northern Finland, Finnmark area of Norway and neighbouring north-western Russia between May 2007 and September 2009 (see also Plomerová *et al.* 2011). The original array consisted of ~ 37 temporary broad-band stations and observatories of the Northern Finland Seismological Network, the Helsinki University Seismic Network and neighbouring stations in Norway. For this study, we enlarge the data set by P-wave arrival times measured on ten permanent stations of the Swedish National Seismological Network located westward of the LAPNET array and two more stations to the north belonging to the Norwegian seismic networks. The extended array covers an area of about 500 km by 500 km with an average inter-station spacing of 70 km (Fig. 4).

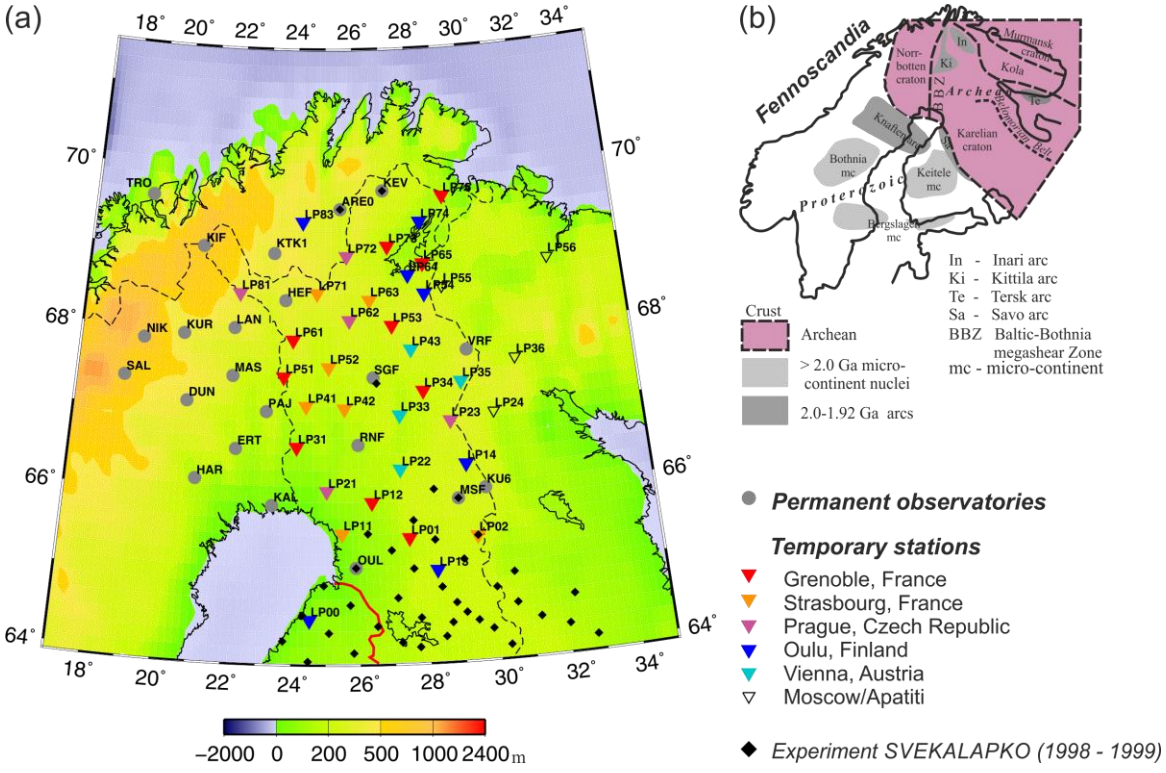

Figure 4. Permanent and temporary seismic stations deployed during passive seismic experiment LAPNET (2007-2009) in northern Fennoscandia (a). Distribution of micro-continental nuclei, island arcs and boundaries of hidden and exposed terranes older than 1.92 Ga in the Fennoscandian Shield (b), redrawn according to Korja *et al.* (2006).

We select recordings of 90 earthquakes from teleseismic epicentral distances between 20º and 100º and measure arrival times of P waves on seismograms with 20 Hz sampling simulating the WWSSN-SP response with the use of a semi-automatic picker developed by Vecsey (private communication 2010), based on Seismic Handler (Stammler 1993).

Because we invert for velocity structure of the upper mantle, we correct the measured travel times for differences between a model of the Fennoscandian crust (Silvennoinen *et al.* 2014) and reference radial velocity model of the Earth IASP'91 (Kennett & Engdahl 1991).

Data pre-processing for the inversion includes a calculation of absolute travel-time residuals, i.e., differences between the observed travel times and the theoretical travel times for reference model IASP'91. To minimize effects originated outside the volume studied, we calculate relative residuals by subtracting an event average residual from the absolute residuals of each event. We also test time stability of the relative residuals to avoid potential operational problems, e.g., occasional failures of the time synchronization at some of the temporary stations. The input P-wave dataset for tomography consists of 3286 relative travel-time residuals, 96 % out of which lie in an interval of (-0.5 s; 0.5 s). Such a low variability of the travel-time residuals excludes a strong large-scale heterogeneity in the upper mantle beneath northern Fennoscandia.

We parametrize the volume studied with an orthogonal 3D grid of nodes, where the horizontal grid spacing is 70 km. Vertical grid nodes are set at 20 km, 50 km and 80 km depth to enhance separation of the mantle lithosphere and the crust. Further down, from 120 km to 370 km the spacing is regular with a 50 km step. AniTomo enables to invert for arbitrarily selected model parameters at each node. According to ray density tensors, describing directional coverage of each grid cell by rays, we define a relatively smooth sub-region at depth layers from 50 km down to 270 km, in which the inversion for all the four anisotropic parameters is allowed. At nodes neighbouring the sub-region at the 50 km - 270 km depths and at all the nodes of the 20 km, 320 km and 370 km depths, we invert only for purely isotropic-velocity perturbations. Thus in total, we invert for 783 perturbations of isotropic-velocity components, 366 perturbations of strength of anisotropy, 366 perturbations of azimuth and 366 perturbations of inclination, i.e., 1881 unknown model parameters all together.

Regarding the initial anisotropic model, we systematically cover the full range of possible initial orientations of the symmetry axis. Therefore, we repeat the inversion 24 times with gridded initial azimuth and inclination within the volume studied. The initial azimuth changes with a step of 45º and the inclination subsequently acquires values of 10º, 45º and 80º. The initial strength of anisotropy is always 0.1 %, the initial 1D reference isotropic-velocity model is IASP'91 (Kennett & Engdahl 1991) and all the inversions consist of 3 iterations. Damping factors are based on synthetic tests.

4.2 Anisotropic tomographic model of the upper mantle beneath northern Fennoscandia

We present the final tomographic model of the anisotropic P-wave velocity of the upper mantle beneath northern Fennoscandia in two figures. Fig. 5 shows perturbations of the isotropic component of the anisotropic velocity (for simplicity referred further as velocity perturbations) at all depths and Fig. 6 shows the complete solution of the anisotropic inversion at the 80 km, 120 km and 170 km depth layers.

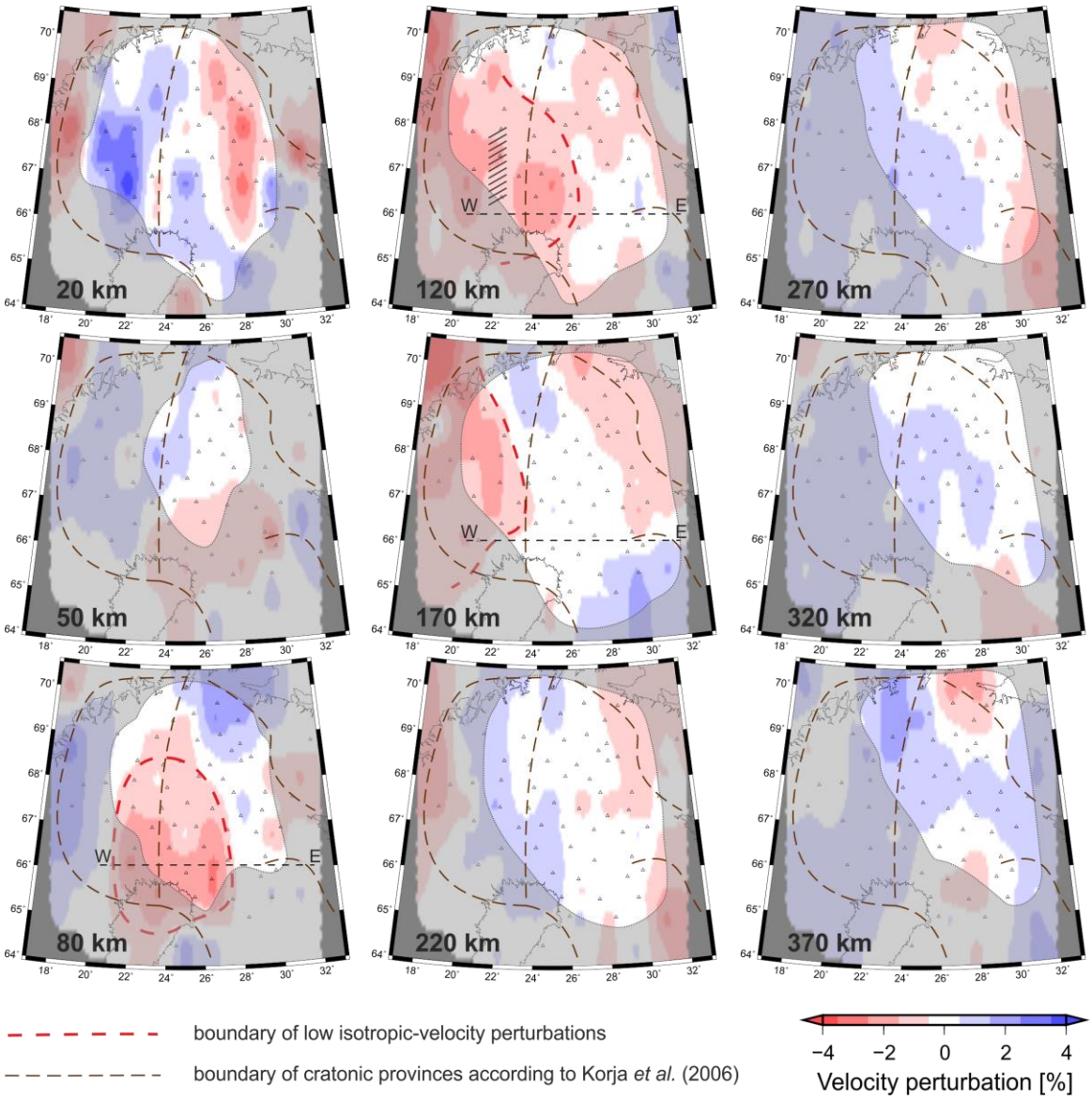

Figure 5. Perturbations of the isotropic velocity calculated as average values of the isotropic-velocity perturbations resulting from the series of the coupled anisotropic-isotropic inversions. Part of the model with RDE < 0.5 is shaded. Red dashed line limits the relatively low-velocity perturbations that dominate western and south-western parts of the model at depths of 80 km, 120 km and 170 km. The hatched area marks a zone of weaker anisotropy and velocity perturbations within Region III at depth of 120 km. The brown dashed curves show boundaries of cratonic provinces after Korja *et al.* (2006); see also Fig. 4. Triangles represent seismic stations of experiment LAPNET together with the nearby permanent stations.

The shallowest layer of the model at the 20 km depth, where only isotropic-velocity perturbations are searched for, is characterized by a great variability of the velocity perturbations with amplitudes larger than 3 % (Fig. 5). The crust, of course, cannot be resolved well by the teleseismic tomography, but this layer absorbs heterogeneities of the thick Fennoscandian crust that are not completely compensated by the model of Moho depths used for a priori corrections of the travel times. Amplitudes of the velocity perturbations decrease at the 50 km depth to about 1 %, confirming thus separation of the

remaining uncorrected crustal structures from the upper mantle. At depths of 80 km and 120 km, the amplitudes increase to 2 %.

The strength of anisotropy reaches more than 3 % on average at 80 km, 120 km and 170 km depths (Fig. 6) and it is possible to delimit regions of consistent anisotropy there (Regions I - V). Negative velocity perturbations of -2 % prevail in the western part of these depth layers and they shift westward with increasing depth. Strength of anisotropy is 3 – 4 % there and, particularly at depths of 120 km and 170 km (Region III), directions of the relatively low velocities dip to the west or north-west, in general. The relatively high velocities lie approximately in a plane steeply dipping to the east or south-east. A sudden change of the anisotropic parameters sharply delimits the eastern boundary of this region. Region III seems to be split into two sub-regions at a depth of 120 km by a zone of weaker anisotropy and velocity perturbations (hatched area in Figs 5 and 6). The part of Region III located eastward of this zone might be related to Region IV, delimited at the 80 km depth (Fig. 6a), in which the high-velocity directions dip to the north-east.

The north-eastern part of the volume exhibits depth dependent anisotropy with strength of about 3 % (Regions I and II; marked with orange in Fig. 6). At the 50 km and 80 km depths, the directions of relatively high velocities tend to dip to the north and the directions of relatively low velocities are perpendicular to that (Region I), while the anisotropic pattern is different at the 120 km and 170 km depths. The directions of relatively low velocities dip to the north-east and the directions of relatively high velocities prevail in a plane dipping to the south-west (Region II).

The very south-eastern part of the 170 km depth layer shows positive-velocity perturbations and directions of relatively high velocity dipping toward the north-east (Region V; marked with blue in Fig. 6). Keeping in mind that resolution of any tomography at its edges is low, we would not rely on the results. However, the anisotropic model with high-velocity *a* axis plunging to the north-east is identical with the fabric derived from both the LAPNET and the SVEKALAPKO data for the Karelian lithosphere, whose thickness attains about 200-220 km in the south-central Finland (Plomerová *et al.* 2006; Vecsey *et al.* 2007).

The model contains also zones of mostly weak and variable anisotropy among the regions with a consistent anisotropy (e.g., Region VI in Fig. 6b). Single-cell anisotropic patterns occur in these zones. A fragmented anisotropic pattern and velocity perturbations below 1 % prevail at depth of 220 km and deeper.

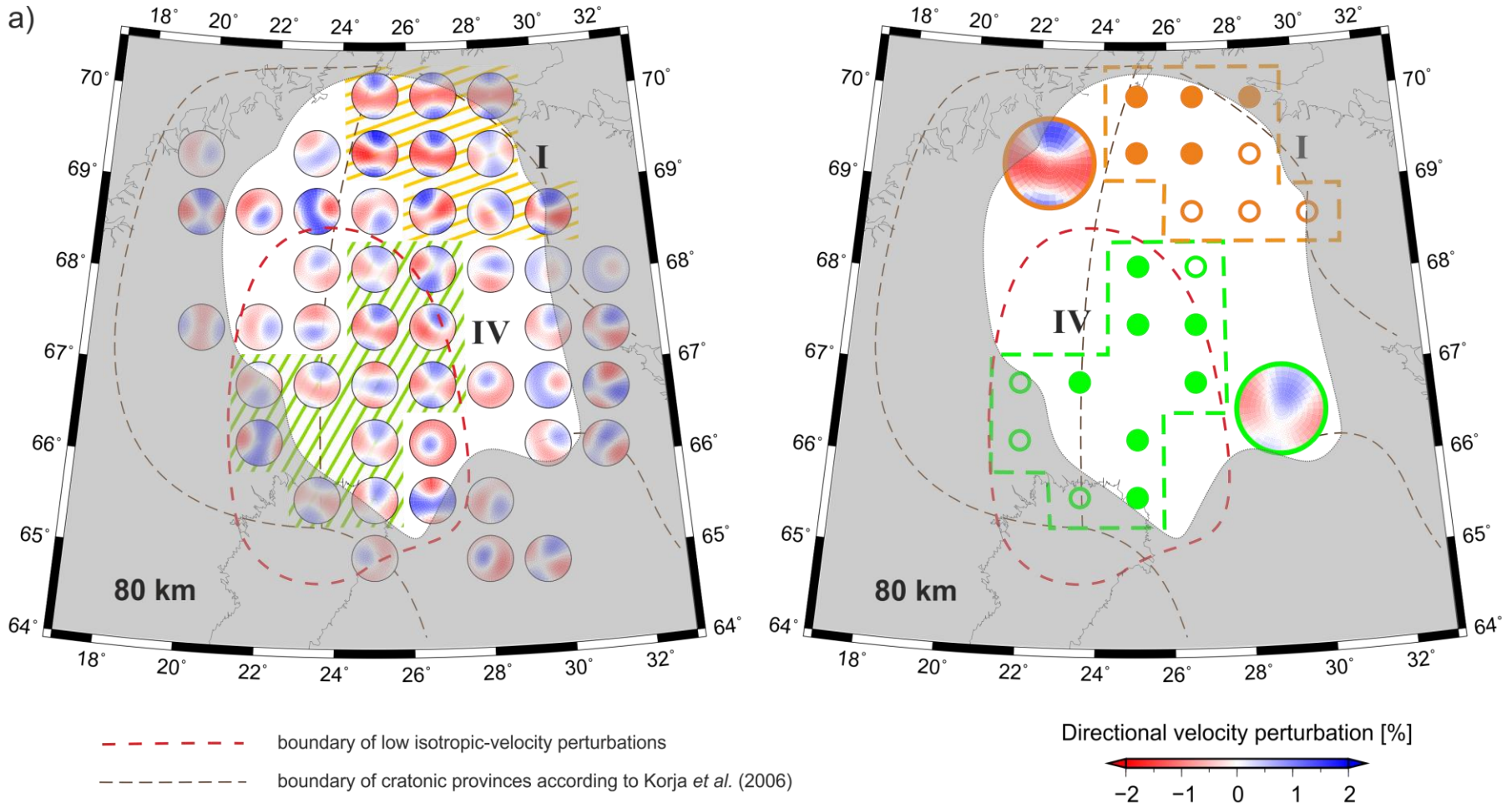

Figure 6. Anisotropic component of P-wave velocities at three selected depth layers. For each grid node we present the anisotropic velocities averaged from the set of individual solutions (left). The anisotropic models are shown only for those nodes, for which at least 8 individual solutions exhibit strength of anisotropy larger than 1 %. Nodes with a similar anisotropic pattern are marked as Regions I-V. A large region with no anisotropy at depth of 120 km is marked as Region VI. The black hatched area locates a zone of weaker anisotropy and velocity perturbations within Region III at depth of 120 km. The typical anisotropic patterns for Regions I-V are shown on the right. Full circles mark nodes, in which the anisotropic pattern matches the typical pattern, while the empty circles mark nodes with only a tendency to the typical pattern. Red dashed curve contours the region with relatively low isotropic-velocity perturbations dominating the model. Part of the model with RDE < 0.5 is shaded. The brown dashed curves show boundaries of cratonic provinces after Korja *et al.* (2006); see also Fig. 4.

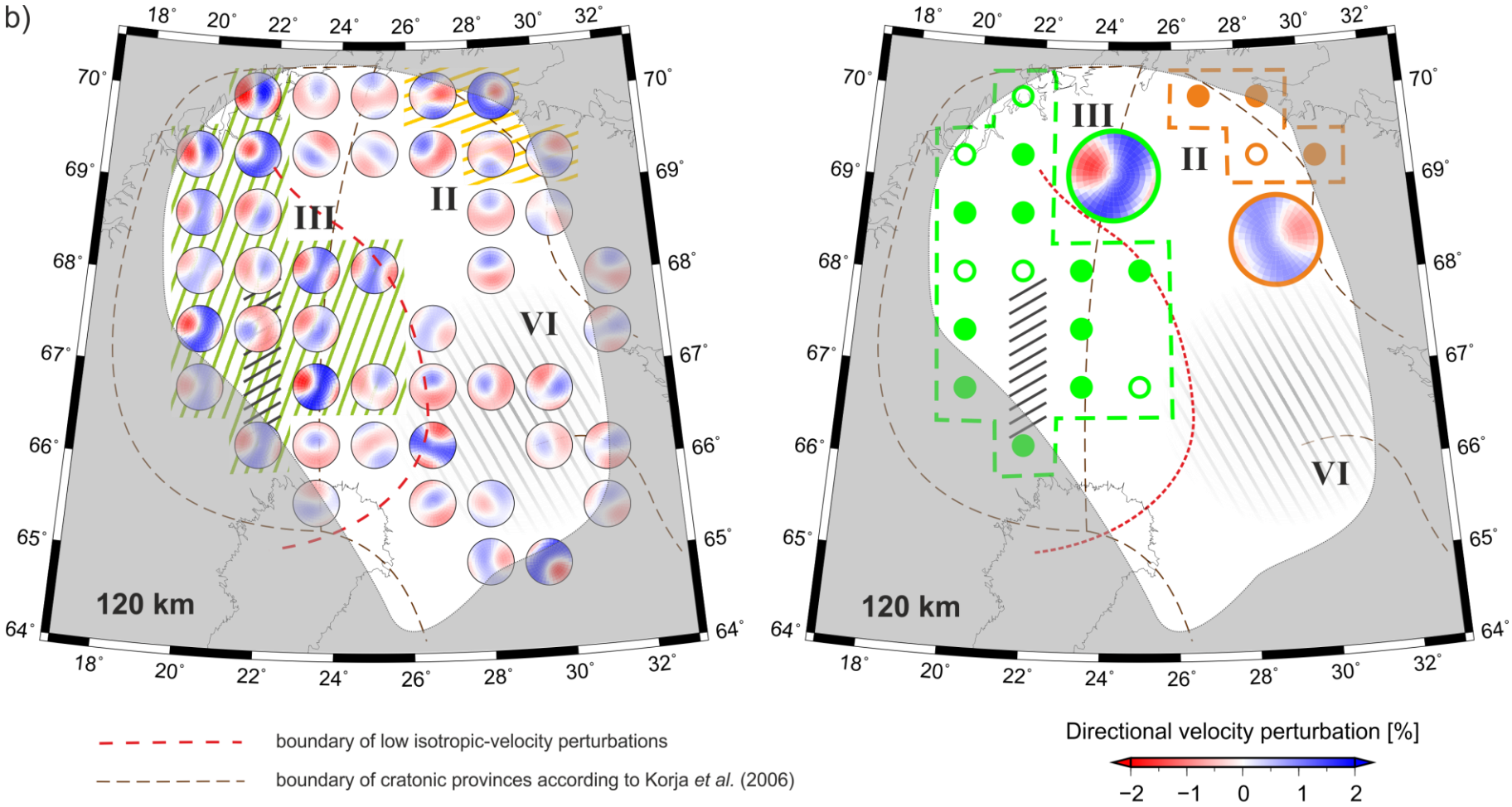

Figure 6. Continue

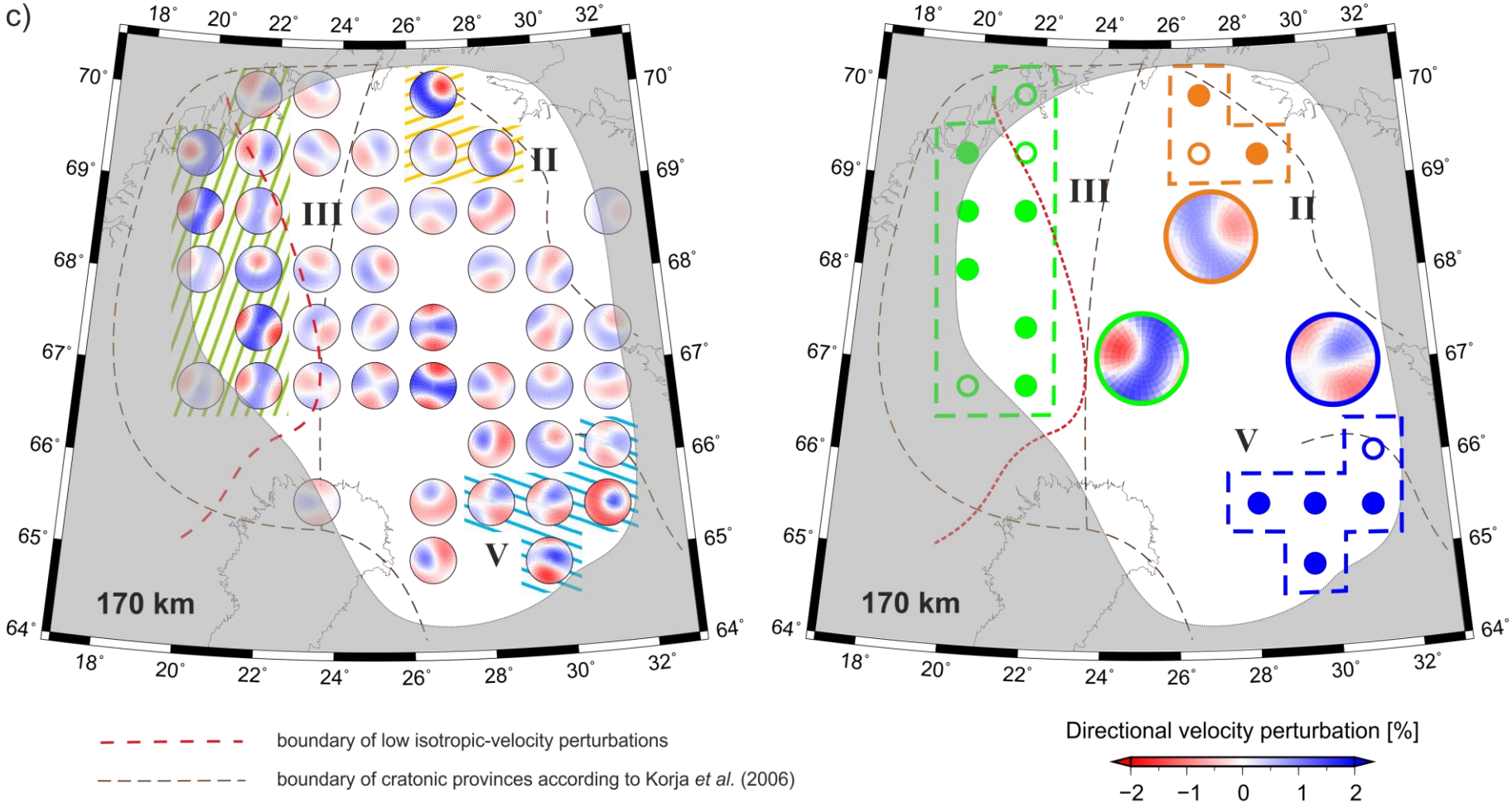

Figure 6. Continue

Regarding a consistency among the models of the velocity perturbations coming out from the set of 24 anisotropic inversions, their standard deviation is lower than 1 % at all the grid nodes and it is even lower than 0.5 % in majority of the nodes. Such a variation of the individual solutions is reasonably low in terms of teleseismic travel-time tomography and it implies robustness of the average values as well. Standard deviations of the velocity perturbations for the LAPNET dataset are comparable with those resulting from various synthetic inversions evaluated for the LAPNET ray geometry. Focusing on the anisotropic part of the model (the strength of anisotropy and orientation of the high- and low-velocity directions), the distribution of the individual solutions creates a systematic pattern at each grid node. This confirms that the task is well determined and the solution is stable. The images of the velocity perturbations from the set of anisotropic inversions (Fig. 5) are almost the same as those from the purely isotropic inversion, which confirms a reliable separation of the isotropic and anisotropic components of the final model.

Reduction of data variance, i.e., (initial variance – final variance) / initial variance, is 60 % for the isotropic-velocity inversion. Evaluation of variance reduction for the coupled anisotropic-isotropic inversion (Fig. 6) is not as straightforward as in the isotropic case, because we can calculate this measure just for each inversion of the set of anisotropic inversions. For the individual anisotropic inversions, the data variance reduction attains values from 61 % to 67 %, which is not a significantly better fit to the P-wave data compared to the fit of the purely isotropic inversion. Nevertheless, the solutions of the individual anisotropic inversions are affected by the initial orientation of the symmetry axis and thus, the fit of a single solution cannot be indeed a representative for the whole coupled anisotropic-isotropic model. Note that the comparison of variance reduction is a poor measure of a quality of the anisotropic results since the two inverse problems (purely isotropic and anisotropic) are significantly and systematically different. By principle it remains unclear how much of the purely isotropic solution is due to a leakage from the ignored anisotropy and for the fully anisotropic solution it needs to be tested how well the separation of parameters is working. In our case, the synthetic tests show that the coupled inversion of purely isotropic input does not create artificial anisotropy.

5. Conclusions

Widely spread detection of seismic anisotropy of the continental mantle lithosphere called for formulating theory and developing novel tomographic code AniTomo that retrieves 3D heterogeneous weakly anisotropic structure of the upper mantle. The code iteratively solves the coupled problem of a 3D anisotropic velocity field by inversion of travel-time residuals of teleseismic P waves for parameters describing weak anisotropy with hexagonal symmetry. The model parameters are perturbations of isotropic component of the anisotropic velocity, strength of anisotropy and azimuth and inclination of the symmetry axis oriented generally in 3D. Current version of AniTomo is applicable only to P waves and not to S waves, for which anisotropic propagation is much more complex.

An extensive testing of the code on realistic synthetic datasets and structures shows, e.g., that the coupled anisotropic-isotropic inversion with AniTomo can successfully distinguish between the isotropic- and anisotropic components of the P-wave velocity even for complex block-like structures of the upper mantle or that the coupled anisotropic-

isotropic inversion does not create anisotropic artefacts when the real structure is purely isotropic.

We apply the AniTomo code for the first time on data recorded during international passive seismic experiment LAPNET (2007 - 2009) in the Archean part of Fennoscandia. We carry out a careful analysis of the ray distribution and document ability of the code to resolve large-scale anisotropic structures in the upper mantle of Fennoscandia by a series of specifically designed synthetic tests.

The tomographic model of P-wave isotropic-velocity perturbations and velocity anisotropy shows that the largest velocity perturbations and the strongest anisotropy concentrate at depth of 80 - 170 km, i.e., in the mantle lithosphere. Below these depths, the lateral velocity variations decrease significantly. According to the modelled anisotropy, which varies both laterally and vertically, the mantle lithosphere of northern Fennoscandia can be divided into several regions exhibiting consistent fabrics. The delimited regions correlate with the tectonic units and their boundaries often correlate with prominent sutures in the crust. The Baltic-Bothnia megashear Zone, the most significant suture zone in the region, seems to have its imprint in the mantle-lithosphere as well.

We identify mantle lithosphere domain associated with the Norrbotten craton, characterized by a distinct anisotropy of about 3 - 4 % strength down to ~ 170 km depth. A relatively complex depth-varying anisotropy in the north-east of the model likely reflects deep structure of various arcs accreted in between the Kola and Norrbotten cratons. The south-eastern part of the tomographic model shows a less consistent large-scale P-wave anisotropy. A small region in the very south-east margin exhibits a fabric similar not only to that revealed by single-station methods from the LAPNET data (Plomerová *et al.* 2011), but also to that in the Karelian mantle lithosphere from data of experiment SVEKALAPKO in south-central Finland (Plomerová *et al.* 2006; Vecsey *et al.* 2007).

Anisotropic tomography retrieves individual regions characterized by consistent, but differently oriented fabrics. The regions are compatible with the domains delimited by joint studies of path-integrated anisotropy from directional analysis of P-wave travel-time residuals and SKS-wave splitting parameters (Plomerová *et al.* 2011). We relate the domain-like anisotropic structure to blocks of Archean mantle lithosphere, which probably preserve their original fossil fabrics. The fabrics mostly survived various tectonic events including the lithosphere domain accretion, as well as the Paleoproterozoic orogenic processes when northern Fennoscandia was formed.

Acknowledgements

The research was supported by grant no. M100121201 of the Czech Academy of Sciences, by grant no. 210/12/2381 of the Grant Agency of the Czech Republic, by grant no. 111-10/253101 of the Grant Agency of Charles University and by project CzechGeo/EPOS-Sci, no. CZ.02.1.01/0.0/0.0/16_013/0001800, financed from the Operational Programme Research, Development and Education within ERDF. Contributions of all members of the LAPNET Working Group are greatly appreciated. Figures were plotted with the use of the Generic Mapping Tools (Wessel & Smith 1998).

I would like to express my sincere gratitude to Jaroslava Plomerová and Eduard Kissling (ETH Zürich) for their inspiring guidance and for their help with emerging problems. Next, I would like to thank Vladislav Babuška, Luděk Vecsey and other colleagues from the Institute of Geophysics and at the Department of Geophysics of the Faculty of Mathematics and Physics for their support during my studies. I also thank all the related working groups for operating passive seismic experiments BOHEMA, RETREAT and LAPNET.

References

Arlitt, R., Kissling, E. & Ansorge, J., 1999. Three-dimensional crustal structure beneath the TOR array and effects on teleseismic wavefronts, *Tectonophysics*, **314**, 309–319.

Babuška, V. & Cara, M., 1991. *Seismic Anisotropy in the Earth*, Kluwer Academic Publishers, Dordrecht, Boston, London.

Babuška, V. & Plomerová, J., 1989. Seismic anisotropy of the subcrustal lithosphere in Europe: another clue to recognition of accreted terranes?, in *Deep structure and past kinematics of accreted terranes*, edited by J. W. Hillhouse, pp. 209-217, Geophys. Monograph 50, IUGG 5, Washington, D. C.

Babuška, V. & Plomerová, J., 1992. The lithosphere in central Europe—seismological and petrological aspects, *Tectonophysics*, **207,** 141–163.

Babuška, V. & Plomerová, J., 2006. European mantle lithosphere assembled from rigid microplates with inherited seismic anisotropy, *Phys. Earth Planet. Inter.* **158,** 264–280.

Babuška, V., Plomerová, J. & Šílený, J., 1984. Spatial variations of P residuals and deep-structure of the European lithosphere, *Geophys. J. R. astr. Soc.*, **79,** 363–383.

Backus, G.E., 1965. Possible forms of seismic anisotropy of the uppermost mantle under oceans, *J. Geophys. Res.*, **70**, 3429-3439.

Bezada, M.J., Faccenda, M. & Toomey, D.R., 2016. Representing anisotropic subduction zones with isotropic velocity models: A characterization of the problem and some steps on a possible path forward, *Geochem. Geophys. Geosyst.*, **17**, 3164–3189, doi: 10.1002/2016GC006507.

Christensen, N.I., 1984. The magnitude, symmetry and origin of upper mantle anisotropy based on fabric analyses of ultramafic tectonites. *Geophys. J. R. Astron. Soc.* **76**, 89-111.

Chyba, J., Plomerová, J., Vecsey, L. & Munzarová, H., 2017. Tomography study of the upper mantle around the TESZ based on PASSEQ experiment data, *Phys. Earth planet. Inter.*, **266**, 29-38. doi.org/10.1016/j.pepi.2017.01.002

Eberhart-Phillips, D. & Henderson, C.M., 2004. Including anisotropy in 3-D velocity inversion and application to Marlborough, New Zealand, *Geophys. J. Int.*, **156** (2), 237–254.

Eken, T., Shomali, H., Roberts, R. & Bödvarsson, R., 2007. Upper mantle structure of the Baltic Shield below the Swedish National Seismological Network (SNSN) resolved by teleseismic tomography, *Geophys. J. Int.*, **169,** 617–630.

Fouch, M.J. & Rondenay, S., 2006. Seismic anisotropy beneath stable continental interiors, *Phys. Earth planet. Inter.*, **158,** 292–320.

Gou, T., Zhao, D., Huang, Z. & Wang, L., 2018. Anisotropic 3-D ray tracing and its application to Japan subduction zone. *J. Geophys. Res. Solid Earth*, **123**, https://doi.org/10.1029/2017JB015321.

Hirahara, K. & Ishikawa, Y., 1984. Travel time inversion for three-dimensional P-wave velocity anisotropy, *J. Phys. Earth*, **32**, 197-218.

Hua, Y., Zhao, D. & Xu, Y., 2017. P wave anisotropic tomography of the Alps, *J. Geophys. Res. Solid Earth*, **122**, 4509–4528, doi:10.1002/2016JB013831.

Ishise, M. & Oda, H., 2005. Three-dimensional structure of P-wave anisotropy beneath the Tohoku district, northeast Japan, *J. Geophys. Res.*, **110**, B07304, doi:10.1029/2004JB003599.

Ishise, M. & Oda, H., 2008. Subduction of the Philippine Sea slab in view of *P*-wave anisotropy, *Phys. Earth planet. Inter.*, **166,** 83–96.
Ishise M., Miyake, H. & Koketsu, K., 2015. Dual subduction tectonics and plate dynamics of central Japan Shown by three- dimensional P-wave anisotropic structure, *Phys. Earth planet. Inter.*, **244**, 49-68, http://dx.doi.org/10.1016/j.pepi.2015.03.008.
Karousová, H., Plomerová, J., & Babuška, V., 2013. Upper-mantle structure beneath the southern Bohemian Massif and its surroundings imaged by high-resolution tomography, *Geophys. J. Int.*, **194**, 1203–1215, doi:10.1093/gji/ggt159.
Karousová, H., Plomerová, J. & Vecsey, L., 2012. Seismic tomography of the upper mantle beneath the north-eastern Bohemian Massif (central Europe), *Tectonophysics*, **564–565,** 1–11.
Kennett, B. & Engdahl, R., 1991. Travel times for global earthquake location and phase identification, *Geophys. J. Int.*, **105**, 429–465.
Kissling, E., 1988. Geotomography with local earthquake data, *Rev. Geophys.*, **26**, 659-698.
Korja, A., Lahtinen, R. & Nironen, M., 2006. The Svekofennian orogen: a collage of microcontinents and island arcs, in *European Lithosphere Dynamics*, pp. 561—578, ed. Gee, D.G. & Stephenson, R.A., Geol. Soc. London, Memoirs, 32.
Koulakov, I., Kukarina, E., Fathi, I., Khrepy, S. & Al-Arifi, N., 2015. Anisotropic tomography of Hokkaido reveals delamination-induced flow above a subducting slab, *J. Geophys. Res.*, **120**, 3219–3239.
Kozlovskaya, E., 2007. Seismic network XK:LAPNET/POLENET seismic temporary array (RESIF-SISMOB). RESIF - Réseau Sismologique et géodésique Français. https://doi.org/10.15778/resif.xk2007
Lahtinen, R., Huhmaa, H., Lahayea, Y., Kousa, J. & Luukas, J., 2015. Archean–Proterozoic collision boundary in central Fennoscandia: Revisited, *Precambrian Research*, **261**, 127-165, http://dx.doi.org/10.1016/j.precamres.2015.02.012.
Lippitsch, R., Kissling, E. & Ansorge, J., 2003. Upper mantle structure beneath the Alpine orogen from high-resolution teleseismic tomography, *J. Geophys. Res.*, **108**, 2376.
Liu, X. & Zhao, D., 2016. Seismic velocity azimuthal anisotropy of the Japan subduction zone: Constraints from P and S wave traveltimes, *J. Geophys. Res.*, **121**, 5086–5115.
Liu, X. & Zhao, D., 2017. P-wave anisotropy, mantle wedge flow and olivine fabrics beneath Japan, *Geophys. J. Int.*, **210**, 1410-1431, doi:10.1093/gji/ggx247.
Long, M.D. & Becker, T.W., 2010. Mantle dynamics and seismic anisotropy, *Earth Planet. Sci. Lett.*, **297**, 341–354.
Long, M.D. & Silver, P.G., 2009. Shear-wave splitting and mantle anisotropy: measurements, interpretations, and new directions, *Surv. Geophys.*, **30,** 407–461.
Mainprice, D., 2007. Seismic anisotropy of the deep Earth from a mineral and rock physics perspective, in *Treatise on Geophysics*, pp. 437--491, ed. Schubert, G., Elsevier, Oxford, U. K.
Maupin, V. & Park, J., 2007. Theory and observations–Wave propagation in anisotropic media, in *Treatise on Geophysics*, vol.1, Seismology and the Structure of the Earth, pp. 289--321, ed. Romanowicz, B. & Dziewonski, A., Elsevier, Boston, Mass., doi:10.1016/B978-044452748-6.00007-9.
Menke, W., 1984. G*eophysical Data Analysis: Discrete Inverse Theory*, 1st edn, Academic Press, Inc., Orlando.
Menke, W., 2015. Equivalent heterogeneity analysis as a tool for understanding the resolving power of anisotropic travel-time tomography, *Bull. Seism. Soc. Am.*, **105**, 719–733.
Park, J. & Levin, V., 2002. Seismic anisotropy: Tracing plate dynamics in the mantle, *Science*, **296**, 485-489, doi:10.1126/science.1067319.
Plomerová, J. & Babuška, V., 2010. Long memory of mantle lithosphere fabric-European LAB constrained from seismic anisotropy, *Lithos*, **120,** 131–143, doi:10.1016/j.lithos.2010.01.008.
Plomerová, J., Babuška, V., Vecsey, L., Kouba, D. & TOR working group, 2002. Seismic anisotropy of the lithosphere around the Trans-European Suture Zone (TESZ) based on teleseismic body-wave data of the Tor experiment, *Tectonophysics*, **360**, 89-114.

Plomerová, J., Babuška, V., Vecsey, L., Kozlovskaya, E., Raita, T. & SSTWG, 2006. Proterozoic-Archean boundary in the upper mantle of eastern Fennoscandia as seen by seismic anisotropy, *J. Geodyn.*, **41**, 400–410, doi:10.1016/j.jog.2005.10.008.

Plomerová, J., Munzarová, H., Vecsey, L., Kissling, E., Achauer, U. & Babuška, V., 2016. Cenozoic volcanism in the Bohemian Massif in the context of P-and S-velocity high-resolution teleseismic tomography of the upper mantle, *Geochem. Geophys. Geosyst.*, **17** (8), 3326–3349, http://dx.doi.org/10.1002/2016GC006318.

Plomerová, J., Vecsey, L., Babuška, V. & LAPNET working group, 2011. Domains of Archean mantle lithosphere deciphered by seismic anisotropy – Inferences from the LAPNET array in northern Fennoscandia, *Solid Earth*, **2**, 303–313, doi:10.5194/se-2-303-2011.

Plomerová, J., Vecsey, L. & Babuška, V., 2012. Mapping seismic anisotropy of the lithospheric mantle beneath the northern and eastern Bohemian Massif (central Europe), *Tectonophysics,* **564–565,** 38–53.

Sandoval, S., Kislling, E., Ansorge, J. & SVEKALAPKO Seismic Tomography working Group, 2004. High-resolution body wave tomography beneath the SVEKALAPKO array - II. Anomalous upper mantle structure beneath the central Baltic Shield, *Geophys. J. Int.*, **157**, 200-214, doi:10.1111/j.1365-246X.2004.02131.x.

Savage, M.K., 1999. Seismic anisotropy and mantle deformation: what have we learned from shear wave splitting?, *Rev. Geophys.*, **37,** 65–106.

Shomali, Z.H., Roberts, R.G., Pedersen, L.B. & the TOR Working Group, 2006. Lithospheric structure of the Tornquist Zone resolved by nonlinear P and S teleseismic tomography along the TOR array, *Tectonophysics,* **416,** 133–149.

Šílený, J. & Plomerová, J., 1996. Inversion of shear-wave splitting parameters to retrieve three-dimensional orientation of anisotropy in continental lithosphere, *Phys. Earth planet. Int.,* **95**, 277–292.

Silvennoinen, H., Kozlovskaya, E., Kissling, E., Kosarev, G. & POLENET/LAPNET working group, 2014. A new Moho boundary map for northern Fennoscandian shield based on combined controlled-source seismic and receiver function data, *Geo. Res. J.*, *1/2*, 19–32.

Silvennoinen, H., Kozlovskaya, E. & Kissling, E., 2016. POLENET/LAPNET teleseismic *P* wave travel time tomography model of the upper mantle beneath northern Fennoscandia, *Solid Earth*, **7**, 425-439, doi:10.5194/se-7-425-2016.

Silver, P.G., 1996. Seismic anisotropy beneath the continents: Probing the depths of geology, *Annu. Rev. Earth Planet. Sci.*, **24**, 385–432, doi:10.1146/annurev.earth.24.1.385.

Silver, P.G. & Chan, W.W., 1991. Shear wave splitting and subcontinental mantle deformation, *J. Geophys. Res.*, **96**, 16429-16454, doi:10.1029/91JB00899.

Slagstad, T., Balling, N., Elvebakk, H., Midttømme, K., Olesen O., Olsen, L. & Pascal, C., 2009. Heat-flow measurements in Late Palaeoproterozoic to Permian geological provinces in south and central Norway and a new heat-flow map of Fennoscandia and the Norwegian–Greenland Sea, *Tectonophysics*, **473**, 341-361.

Sobolev, S., Gresillaud, A. & Cara, M., 1999. How robust is isotropic delay time tomography for anisotropic mantle?, *Geophys. Res. Lett.*, **26** (4), 509–512.

Snyder, D.B., 2002. Lithospheric growth at margins of cratons, *Tectonophysics*, **355**, 7-22.

Stammler, K., 1993, Seismic handler programmable multichannel data handler for interactive and automatic processing of seismological analyses, *Comput. Geosci.*, **19**, 135–140, doi:10.1016/0098-3004(93)90110-Q.

Steck, L.K. & Prothero, W.A., 1991. A 3-D ray-tracer for teleseismic body-wave arrival-times, *B. Seismol. Soc. Am.*, **81**, 1332-1339.

Tian, Y. & Zhao, D., 2013. Reactivation and mantle dynamics of North China Craton: Insight from P-wave anisotropy tomography, *Geophys. J. Int.*, **195**, 1796–1810.

Vecsey, L., Plomerová, J., Kozlovskaya, E. & Babuška, V., 2007. Shear-wave splitting as a diagnostic of varying upper mantle structure beneath south-eastern Fennoscandia, *Tectonophysics,* **438**, 57–77, doi:10.1016/j.tecto.2007.02.017.

Wang, J. & Zhao, D., 2008. P-wave anisotropic tomography beneath Northeast Japan, *Phys. Earth planet. Inter.*, **170**, 115–133.

Wang, J. & Zhao, D., 2012. P wave anisotropic tomography of the Nankai subduction zone in Southwest Japan, *Geochem. Geophys. Geosyst.*, **13**, Q05017.

Weiland, C.M., Steck, L.K., Dawson, P.B. & Korneev, V.A., 1995. Nonlinear teleseismic tomography at Long Valley caldera, using three-dimensional minimum travel time ray tracing, *J. Geophys. Res.*, **100**, 20379–20390.

List of author's publications

Munzarová, H., Plomerová, J., Kissling, E., Vecsey, L. & Babuška, V., 2018. Novel anisotropic teleseismic body-wave tomography code AniTomo to illuminate heterogeneous anisotropic upper mantle: Part II - Application to data of passive seismic experiment LAPNET in northern Fennoscandia, *Geophys. J. Int.*, **215** (2), 1388-1409, doi:10.1093/gji/ggy327.

Munzarová, H., Plomerová, J. & Kissling, E., 2018. Novel anisotropic teleseismic body-wave tomography code AniTomo to illuminate heterogeneous anisotropic upper mantle: Part I – Theory and inversion tuning with realistic synthetic data, *Geophys. J. Int.*, **215** (1), 524-545, doi:10.1093/gji/ggy296.

Vecsey, L., Plomerová, J., Jedlička, P., **Munzarová, H.** & Babuška, V., 2017. Data quality control and tools in passive seismic experiments exemplified on the Czech broadband seismic pool MOBNET in the AlpArray collaborative project, *Geosci. Instrum. Method. Data Syst.*, **6**, 505-521, doi:10.5194/gi-6-505-2017.

Chyba, J., Plomerová, J., Vecsey, L. & **Munzarová, H.**, 2017. Tomography study of the upper mantle around the TESZ based on PASSEQ experiment data, *Phys. Earth Planet. Int.*, **266**, 29-38, doi:10.1016/j.pepi.2017.01.002.

Plomerová, J., **Munzarová, H.**, Vecsey, L., Kissling, E., Achauer, U. & Babuška, V., 2016. Cenozoic volcanism in the Bohemian Massif in the context of P-and S-velocity high-resolution teleseismic tomography of the upper mantle, *Geochem. Geophys. Geosyst.*, **17** (8), 3326–3349, doi:10.1002/2016GC006318.

Munzarová, H., Plomerová, J., Babuška, V. & Vecsey, L., 2013. Upper-mantle fabrics beneath the Northern Apennines revealed by seismic anisotropy, *Geochem. Geophys. Geosyst.*, **14**, 1156–1181, doi:10.1002/ggge.20092.